Research Square

Preprints are preliminary reports that have not undergone peer review.
They should not be considered conclusive, used to inform clinical practice,
or referenced by the media as validated information.

Absorber Doping Controls Internal Electric Field and Transport- Recombination Trade-Off in Perovskite Solar Cells: A SILVACO ATLAS TCAD Study

Aly Touré

aly.toure1@univ-thies.sn

UFR Sciences and Technologies, Iba Der Thiam University of Thies, VCN

Fatma Sow

UFR Sciences and Technologies, Iba Der Thiam University of Thies, VCN

Dimitry Diassy

UFR Sciences and Technologies, Iba Der Thiam University of Thies, VCN

Ahmed Mohamed-Yahya

University of Nouakchott

Mamadou Lamine Samb

UFR Sciences and Technologies, Iba Der Thiam University of Thies, VCN

Research Article

Keywords: Perovskite solar cell, SILVACO ATLAS, Absorber doping, Internal electric field, Carrier Recombination

Posted Date: October 6th, 2026

DOI: https://doi.org/10.21203/rs.3.rs-11253484/v1

License: This work is licensed under a Creative Commons Attribution 4.0 International License.
Read Full License

Additional Declarations: No competing interests reported.

Absorber Doping Controls Internal Electric Field and Transport-Recombination Trade-Off in Perovskite Solar Cells: A SILVACO ATLAS TCAD Study

Aly Touré[1*], Fatma Sow[1], Dimitry Diassy[1], Ahmed Mohamed-Yahya[2] and Mamadou Lamine Samb[1]

[1]*Department of Physics-Chemistry, UFR Sciences and Technologies, Iba Der Thiam University of Thies, VCN, BP 967, Thies, Senegal;*
aly.toure1@univ-thies.sn, fatma.sow@univthies.sn; dimitry.diassy@univthies.sn; mlsamb@univ-thies.sn
[2]*Applied Research Unit for Renewable Energies, University of Nouakchott, Nouakchott, BP 5026, Mauritania*
biyah2001@yahoo.fr
Corresponding author: Aly Touré; aly.toure1@univ-thies.sn; https://orcid.org/0009-0009-9736-7733

Abstract:
Perovskite solar cells combine strong optical absorption with favorable carrier-transport properties, but their performance remains highly sensitive to the electrical properties of the absorber, particularly its doping level. In this work, SILVACO ATLAS TCAD is used to investigate how absorber doping modifies the electrical response of a planar $CH_3NH_3PbI_3$ absorber layer in an $ITO/NiO/CH_3NH_3PbI_3/ZnO/Au$ architecture. Photovoltaic parameters, including open-circuit voltage (V_{oc}), short-circuit current density (J_{sc}), fill factor (FF), efficiency (η), together with effective series and shunt resistances, were extracted from the simulated current–voltage characteristics. Spatially resolved energy-band bending, electrostatic potential, internal electric field, photogeneration, and recombination profiles were then analyzed to connect the microscopic electrostatic response to the macroscopic photovoltaic behavior. The results show that a doping concentration of $5 \times 10^{16}\ cm^{-3}$ provides the compromise between carrier transport, resistive losses, and recombination, yielding a maximum efficiency of 23.35%. Two competing regimes emerge: from low to intermediate doping, improved conductivity and interfacial electrostatics enhance charge extraction, whereas at high doping, field localization and strongly increased bulk recombination progressively reduce carrier collection despite continued gains in some voltage- and fill-factor-related indicators. Because photogeneration remains essentially unchanged, the efficiency optimum results from a transport-recombination trade-off rather than an optical effect

Keywords: Perovskite solar cell; SILVACO ATLAS; Absorber doping; Internal electric field; Carrier Recombination.

1. Introduction

The increase in global energy demand and growing environmental concerns have significantly accelerated the development of next-generation photovoltaic technologies. Among them, perovskite solar cells have attracted considerable attention due to their excellent optical and electronic properties, including a high absorption coefficient, low exciton binding energy, high carrier mobility, and low-cost manufacturing processes [1, 2]. In just a few years, their conversion efficiency has risen from under 4% to over 23%, making this technology one of the most promising for future photovoltaic applications [3, 4].

Despite these remarkable performances, the electrical properties of perovskite cells remain heavily influenced by design parameters, particularly the doping level of the absorber layer. This parameter simultaneously modifies the internal electric field, recombination mechanisms, carrier transport, and resistive losses represented by series resistance (R_s) and shunt resistance (R_{sh}), which directly condition the open-circuit voltage (V_{oc}), short-circuit current density (J_{sc}), fill factor (FF), and overall efficiency.

This study uses the SILVACO ATLAS TCAD simulator to evaluate the influence of absorber-layer doping on the photovoltaic response of a planar perovskite solar cell [5], with particular attention to R_s and R_{sh} and their correlation with the photovoltaic parameters and spatially resolved loss mechanisms.

Rather than treating absorber doping only as an optimization variable, this work examines it as an electrostatic control parameter that redistributes the potential drop, internal electric field, and carrier-collection conditions throughout the heterostructure. The contribution therefore lies in a correlated interpretation of energy-band bending, electrostatic potential, internal-field distribution, photogeneration, recombination, and effective resistive losses. This framework is used not only to identify an optimal doping range, but also to clarify the transition from a regime in which improved conductivity and carrier extraction dominate to a regime in which recombination losses increasingly govern the device response.

2. Modeling of the Solar Cell

2.1. Equivalent Electrical Circuit

The electrical behavior of a photovoltaic solar cell is described by an equivalent model coupling a photogenerated current source in parallel with a diode, complemented by a series resistance R_s (bulk and contact ohmic losses) and a shunt resistance R_{sh} (parasitic leakage and recombination pathways) [6, 7, 8]. **Figure 1** illustrates this equivalent circuit of a solar cell used for analyzing I-V characteristics.

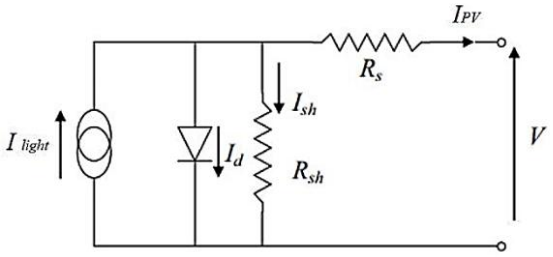


Figure 1 : Equivalent circuit of a photovoltaic solar cell

By applying Kirchhoff's current law to the equivalent circuit, the current supplied by the cell is written as:

$$I_{PV} = I_{light} - I_d - I_{sh} \quad (1)$$

Where: I_{PV}: current supplied by the cell. Ilight, current generated by illumination (photocurrent); I_{sh}: current through the shunt resistor; I_d: diode current (dark current).

The voltage-current relationship in the shunt branch leads to:

$$I_{Sh}.R_{Sh} - I_{PV}.R_S - V = 0 \quad (2)$$

Where: I_{PV}: current supplied by the cell. Ilight: current generated by illumination (photocurrent). I_{sh}: current through the shunt resistor; I_d: diode current (dark current).

And the diode current is classically described by:

$$I_d = I_0 \left[\exp\left(\frac{V_D}{AV_t}\right) - 1\right] \quad (3)$$

Where: I_0 : reverse saturation current of the diode; A: ideality factor of the material (typically between 1 and 2); $V_t = \frac{KT}{q}$: thermal voltage; V_D : voltage across the diode; T: temperature in Kelvin; k: Boltzmann constant (1.38×10^{-23} J/K); q: elementary charge (1.602×10^{-19} C).

By combining equations (1) and (3), we obtain the standard expression for the single-diode model [8, 9,10].

$$I_{PV} = I_{Light} - I_0 \left[\exp\left(\frac{qV + q(I_{PV}.R_S)}{A.K_B.T}\right) - 1\right] - \left(\frac{V + (I_{PV}.R_S)}{R_{Sh}}\right) \quad (4)$$

2.2. Photovoltaic Parameters

The current-voltage relationship of an illuminated photovoltaic cell allows the extraction of key performance parameters, such as the open-circuit voltage (V_{oc}), short-circuit current density (J_{sc}), fill factor (FF), and power conversion efficiency (η) [11, 12, 13].

- *The Short-Circuit Current* I_{sc}*:* The short-circuit current is obtained when the applied voltage is zero. It is defined as:

$$I_{cc} = I_s \left[\exp\left(\frac{qV}{KT}\right) - 1\right] \quad (5)$$

- *The Open-Circuit Voltage* V_{oc} *:* It corresponds to the voltage delivered when the net current is zero (I = 0) [14].

$$V_{oc} = \frac{nKT}{q}.\ln\left(\frac{I_{ph}}{I_s} + 1\right) \quad (6)$$

Where: I_{ph} : photogenerated current; I_0 : reverse saturation current

- *The Maximum Power* P_{max}*:* It represents the maximum electrical power produced by the cell under irradiance. It is associated with the maximum voltage (V_{max}) and current (I_{max}) operating points:

$$P_{max} = V_{max} \times I_{max} \quad (7)$$

- *The Fill Factor (FF):* The fill factor is a dimensionless parameter that reflects the electrical quality of a photovoltaic cell. It serves as a measure of the squareness of the J-V characteristic curve. The FF depends on the design of the cell, the quality of the p-n junction, the properties of the raw materials, and the resistivity of the metallic contacts [15, 16]. It is defined by the following expression:

$$FF = \frac{P_{max}}{V_{oc}.I_{cc}} \quad (8)$$

- *The Power Conversion Efficiency (η):* It represents the ratio between the maximum power supplied by the device and the incident light power (P_{inc}, defined per unit area), and can be enhanced by simultaneously increasing the fill factor, the short-circuit current density, and the open-circuit voltage [17].

$$\eta = \frac{P_{max}}{P_{inc}.S} = \frac{V_{max}.I_{max}}{P_{inc}.S} = FF.\frac{V_{oc}.I_{ph}}{P_{inc}.S} \quad (9)$$

Where: P_{inc} : incident light power density (usually 100 mW/cm^2 or 1000 W/m^2 under standard AM1.5G spectrum); S: active surface area of the cell.

Series Resistance (R_s*):* The series resistance is a parameter extracted from the differential slope of the I-V curve near the open-circuit voltage condition [18, 19]:

$$R_s = \left(\frac{dV}{dI}\right)_{V \to V_{oc}} \quad (10)$$

From a physical perspective, the series resistance (R_s) aggregates the cumulative ohmic resistances of the individual charge transport layers, bulk regions, and metallic contact interfaces. Its effect on the J-V curve manifests as an internal voltage drop ($\Delta V = IR_s$), which directly chokes the extracted electrical power, particularly near the maximum power point.

Shunt Resistance (R_{sh}): The shunt (or parallel) resistance (R_{sh}) represents the equivalent resistance associated with all alternative parasitic leakage current pathways across the junction [17, 18]. Its influence is revealed through a parasitic loss of current ($\Delta I = R_{sh}.V$), which degrades both the open-circuit voltage (V_{oc}) and the fill factor (FF). It is defined as :

$$R_{sh} = \left(\frac{dV}{dI}\right)_{I \to I_{sc}} \quad (11)$$

In the present numerical analysis, the series and shunt resistances are treated as effective electrical quantities extracted from the simulated illuminated current-voltage characteristics. Their evolution with absorber doping should therefore not be interpreted as the direct variation of externally imposed circuit elements. Instead, the extracted values reflect the global response of the simulated device to changes in carrier transport, recombination, conductivity, and leakage-related losses. Consequently, the analysis of R_s and R_{sh} is combined with the spatial distributions of the electrostatic potential, internal electric field, and recombination rate in order to distinguish the effective electrical response of the complete heterostructure from a direct modification of an individual material resistance.

3. Physical Models Used in ATLAS

The Poisson equation relates the electrostatic potential (ψ) to the local space charge density (ρ) inside an electronic device:

$$\mathrm{div}(\varepsilon \nabla \psi) = -\rho \quad (12)$$

Where ε is the local permittivity.

$$\mathrm{div}(\nabla \psi) = \Delta \psi = -\frac{q}{\varepsilon}[p - n + N_D^+ - N_A^-] \quad (13)$$

It accounts for the free carriers, namely electrons (n) and holes (p), as well as ionized impurities, including donors (N_D^+) and acceptors (N_A^-).

- *Carrier Continuity Equations:* The continuity equations for electrons and holes are defined by the following expressions:

$$\frac{\partial n}{\partial t} = \frac{1}{q}\mathrm{div}\overrightarrow{J_n} + G_n - R_n \quad (14)$$

$$\frac{\partial p}{\partial t} = -\frac{1}{q}\mathrm{div}\overrightarrow{J_p} + G_p - R_p \quad (15)$$

Where n and p represent electron and hole concentrations respectively, J_n and J_p are the electron and hole current densities, G_n and G_p are the generation rates for electrons and holes, and R_n and R_p are the recombination rates for electrons and holes. The current densities are given by:

$$\vec{J}_n = qn\mu_n\vec{E}_n + qD_n\nabla n \quad (16)$$

$$\vec{J}_p = qp\mu_p\vec{E}_p - qD_p\nabla p \quad (17)$$

With :

$$\vec{E}_n = -\nabla\left(\psi + \frac{kT}{q}\ln(n_{ie})\right) \quad (18)$$

$$\vec{E}_p = -\nabla\left(\psi - \frac{kT}{q}\ln(n_{ie})\right) \quad (19)$$

4. Device Structure

The investigated solar cell is a planar heterostructure perovskite solar cell consisting of a transparent conductive oxide anode (ITO), a hole-transport layer (NiO), a $CH_3NH_3PbI_3$ perovskite absorber layer, an electron transport layer (ZnO), and a gold metallic cathode (Au). This architecture promotes efficient separation of photogenerated carriers due to an optimized energy alignment between the adjacent functional layers.

The perovskite absorber layer ($CH_3NH_3PbI_3$) constitutes the active region of the cell. Its doping concentration varies from 10^{13} to 10^{18} cm^{-3} to evaluate its effect on photovoltaic performance.

Simulations are carried out using the ATLAS simulator from SILVACO TCAD software, which numerically solves the Poisson equation and the carrier continuity equations [5], yielding the internal distributions of electrostatic potential, energy bands, carrier concentrations, and recombination rates. The architecture of the studied device is illustrated in **Figure 2.**

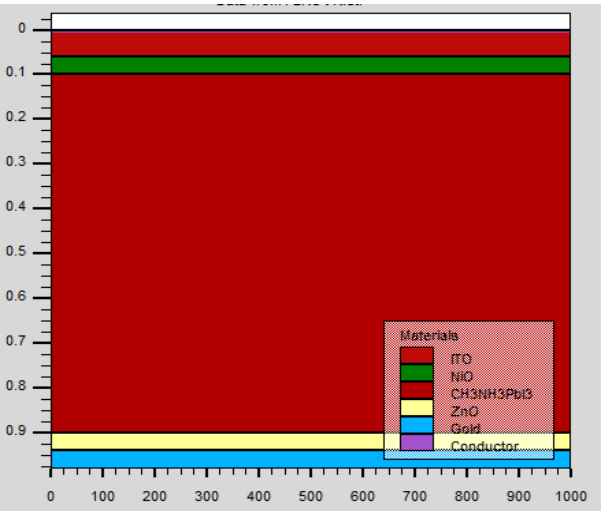


Figure 2 : Structure of the investigated solar cell: ITO/NiO/$CH_3NH_3PbI_3$/ZnO/Au

5. Material Parameters

The physical properties of the semiconductor materials are extracted from established literature data. The simulation study using SILVACO TCAD-ATLAS software requires entering the precise physical parameters of each constituent layer of the investigated solar cell structure [19, 20, 21].

Table I : Physical parameters used in the simulation

Parameters	**ITO**	**NiO**	**$CH_3NH_3PbI_3$**	**ZnO**
Bandgap E_g (eV)	3.5	3.5	1.585	3.3
Electron affinity χ (eV)	2.3	2.2	3.9	4.0
Permittivity ε	9.0	9.0	3.9	8.5
Effective conduction band density of states N_c (cm^{-3})	2.2×10^{18}	2×10^{18}	2.2×10^{18}	4×10^{18}
Effective valence band density of states (cm^{-3})	1.8×10^{19}	1.9×10^{19}	1.8×10^{19}	1.8×10^{19}
Electron mobility μ_n ($cm^2/V \cdot s$)	30	1	5	100

Hole mobility μ_p ($cm^2/V \cdot s$)	5	0.5	5	30
Electron lifetime τ_n (s)	10^{-5}	10^{-5}	10^{-5}	10^{-5}
Hole lifetime τ_p (s)	10^{-5}	10^{-5}	10^{-5}	10^{-5}
Diffusion length (μm)	0.06	0.04	0.8	0.04

The defects present within the perovskite absorber bulk layer ($CH_3NH_3PbI_3$) are detailed in **Table 2** below.

Table II :"Simulation parameters for defect state densities and carrier capture cross-sections.

Defect Parameters	**Gaussian Acceptor (A) States**	**Gaussian Donor (D) States**
Gaussian distribution density N_{GA}, N_{GD} (cm^{-3})	10^{16}	10^{16}
Tail distribution density N_{TA}, N_{TD} (cm^{-3})	1.10^{18}	1.10^{18}
Peak energy level E_{GA}, E_{GD} (eV)	0.75	0.85
Gaussian distribution width W_{GA}, W_{GD} (eV)	0.08	0.08
Tail distribution width W_{TA}, W_{TD} (eV)	0.025	0.025
Electron/Hole capture cross-section σ (cm^2)	1.10^{-14}	1.10^{-14}

Solar cell simulations are performed under standard operating conditions (AM1.5G, 100 mW/cm², and 300 K). The conmob and fldmob models account for the dependence of carrier mobility on doping concentration and local electric-field intensity, while Shockley-Read-Hall (SRH) and Auger mechanisms describe non-radiative and high-carrier-density recombination. Fermi–Dirac statistics and the optical generation model (optr) complete the simulation framework. Together, these models provide a physically consistent description of the coupled transport, generation, and recombination processes considered in the present analysis.

The effect of absorber doping is analyzed hierarchically. The macroscopic photovoltaic response is first established, after which its physical origin is examined through the redistribution of energy bands, electrostatic potential, internal electric field, recombination, and photogeneration profiles. This sequence makes it possible to distinguish optical generation, which remains nearly unchanged, from doping-induced variations in carrier transport, collection, and recombination, and thereby to connect the microscopic electrostatic response to the observed evolution of V_{oc}, J_{sc}, FF, and η.

6. Results and Discussion

6.1. Band diagram of the PV cell: $ITO/NiO/CH_3NH_3PbI_3/ZnO/Au$

Figure 3 illustrates the energy band diagram of the $ITO/NiO/CH_3NH_3PbI_3/ZnO/Au$ solar cell under three distinct doping concentrations of the perovskite absorber layer: $10^{15}, 5 \times 10^{16}$ et 10^{18} cm^{-3}. The red curves correspond to the conduction band (E_c), while the blue curves represent the valence band (E_v).

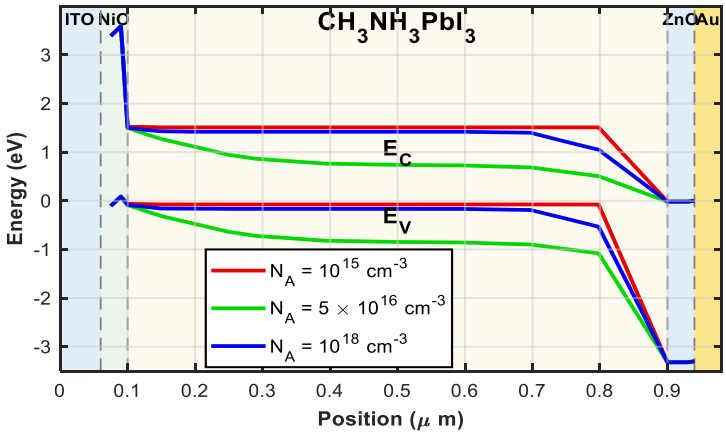


Figure 3 : Energy band diagram of the ITO/NiO/ $CH_3NH_3PbI_3$ solar cell

The analysis reveals that at the ITO/NiO interface, the three diagrams are nearly superimposed, indicating that the absorber doping does not significantly perturb the electronic properties of the adjacent transport layers, with a band discontinuity at the NiO/perovskite interface that remains practically constant, guaranteeing efficient hole extraction while suppressing minority electron leakage.

The most substantial modifications occur within the bulk of the absorber layer ($CH_3NH_3PbI_3$). At a low doping concentration of 10^{15} cm^{-3}, the bands exhibit pronounced bending over a relatively large fraction of the absorber, indicating that the electrostatic potential drop is distributed over a wider active volume. This extended electrostatic driving force can assist carrier separation and directional transport while maintaining comparatively low bulk recombination.

When the doping density is increased to 5×10^{16} cm^{-3}, the band bending is redistributed rather than simply suppressed. The device retains sufficient electrostatic driving force for charge separation, while the spatial balance between drift-assisted collection, conductivity, and doping-induced recombination becomes more favorable. This intermediate regime therefore provides the best global compromise and coincides with the maximum conversion efficiency observed at this concentration [22, 23, 24].

For the highly doped case 10^{18} cm^{-3}, the energy bands become substantially flatter across much of the perovskite bulk, while the potential variation becomes increasingly confined to the heterointerfacial regions. The corresponding contraction of the space-charge region leaves a larger quasi-neutral bulk in which carrier transport is predominantly diffusion-assisted. Carriers generated far from the selective interfaces must therefore rely more strongly on their diffusion length and lifetime, increasing their susceptibility to non-radiative losses; this penalty is further amplified by the stronger SRH and Auger recombination observed at high carrier density.

At the $CH_3NH_3PbI_3$/ZnO interface, the three configurations maintain a small conduction-band offset that does not create a major energetic barrier for electron transfer into the ETL. At high doping, however, the bulk potential gradient is reduced and increasingly localized near the interface. Electron injection therefore remains energetically accessible, but the overall collection probability deteriorates because a larger fraction of the absorber becomes weakly field-assisted and more vulnerable to recombination.

6.2. Electrostatic potential of the PV cell: $ITO/NiO/CH_3NH_3PbI_3/ZnO/Au$

Figure 4 highlights the spatial distribution of the electrostatic potential across the $ITO/NiO/CH_3NH_3PbI_3/ZnO/Au$ heterostructure under three distinct acceptor doping levels (10^{15}, 5×10^{16}, and 10^{18} cm^{-3}) of the perovskite active layer.

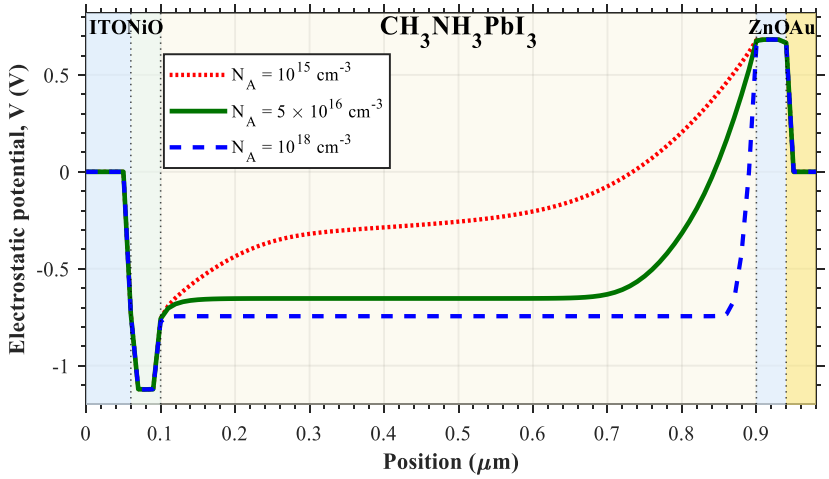


Figure 4 : Electrostatic potential profile across the ITO/NiO/ $CH_3NH_3PbI_3$/ZnO/Au heterostructure for different absorber doping concentrations

The analysis of **Figure 4** reveals sharp potential gradients localized primarily at the ITO/NiO and $CH_3NH_3PbI_3/ZnO$ interfaces, whereas the potential remains relatively uniform throughout a significant portion of the bulk $CH_3NH_3PbI_3$ layer. At a low doping density of 10^{15} cm^{-3}, the electrostatic potential exhibits a gradual and progressive transition within the perovskite bulk, scanning from -0.8 V to 0.7 V, reflecting a built-in field distributed across a wider active volume. Conversely, as the doping concentration increases to 5×10^{16} cm^{-3} and subsequently to 10^{18} cm^{-3}, the potential locks onto a nearly constant plateau throughout the majority of the absorber bulk, before undergoing a steep, abrupt rise in the immediate vicinity of the $CH_3NH_3PbI_3/ZnO$ interface. This spatial concentration of the potential drop confirms a localized enhancement of band bending and a severe shrinkage of the space charge region (SCR) toward the selective hetero-interface.

This is consistent with semiconductor doping physics, which sharpens the electrostatic junction profile at the $CH_3NH_3PbI_3/ZnO$ interface, directly correlated with the internal electric field via $\left(E = -\frac{dV}{dx}\right)$: regions of rapid potential variation correspond to zones of intense local field. Under intermediate and high doping, the steep potential gradient near the ZnO layer therefore reflects a strongly localized interfacial field, whereas at low doping the potential drop is distributed over a broader portion of the absorber. The distinction is thus not simply between a "weak" and a "strong" internal field, but between an extended electrostatic driving force at low doping and an increasingly localized interfacial field as the acceptor density rises [26, 27, 28].

6.3. Internal electric field of the PV cell: $ITO/NiO/CH_3NH_3PbI_3/ZnO/Au$

Figure 5 presents the spatial distribution of the internal electric field (E) within the $ITO/NiO/CH_3NH_3PbI_3/ZnO/Au$ heterostructure under three distinct perovskite acceptor doping levels $10^{15}, 5 \times 10^{16}$ et 10^{18} cm^{-3}.

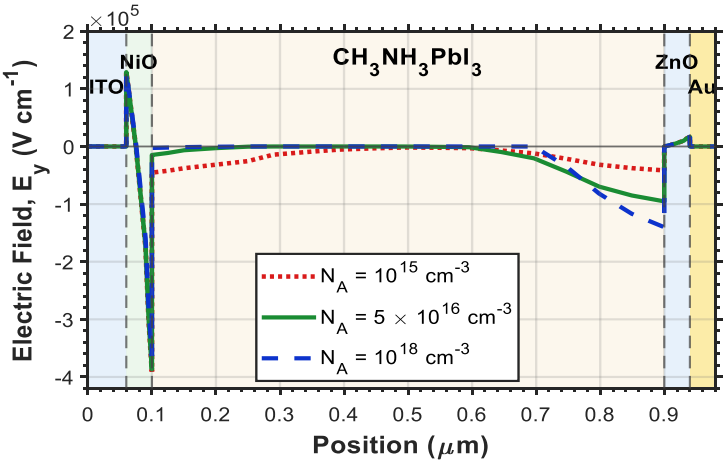


Figure 5 : Internal electric-field distribution across the ITO/NiO/$CH_3NH_3PbI_3$/ZnO/Au heterostructure for absorber acceptor concentrations

The investigation of the field profiles clearly indicates that all three configurations exhibit a globally similar trend, characterized by pronounced field spikes localized in the immediate vicinity of the hetero-interfaces, contrasting with a relatively weak electric field across the bulk of the perovskite absorber. At the anodic $NiO/CH_3NH_3PbI_3$ interface 0,1 µm, the internal electric field reaches its absolute extremum, peaking in magnitude at approximately $(-3.9 \times 10^5\ \mathrm{V.cm^{-1}})$, before undergoing a sharp spatial transition that establishes a robust space charge region (SCR), coupled with the interfacial band bending driving carrier dissociation and drift before early recombination.

Within the central bulk region of the perovskite layer, spanning approximately from 0.15 µm *to* 0.72 µm, the internal electric field decays sharply and vanishes toward zero ($E \approx 0\ \mathrm{V.cm^{-1}}$), confirming an electrostatically quasi-neutral zone where transport becomes increasingly diffusion-dominated as the field approaches zero. Conversely, at the cathodic ($CH_3NH_3PbI_3/ZnO$) interface (0.895 µm), the electric field drops into negative values, reaching local minima of $-0{,}45 \times 10^5\ \mathrm{V.cm^{-1}}$, $-0{,}95 \times 10^5\ \mathrm{V.cm^{-1}}$ and $-1{,}4 \times 10^5\ \mathrm{V.cm^{-1}}$ for doping densities of $10^{15}\ \mathrm{cm^{-3}}$, $5 \times 10^{16}\ \mathrm{cm^{-3}}$ and $10^{18}\ \mathrm{cm^{-3}}$, respectively a regular increase reflecting redistribution of ionised acceptors near the n-i junction that accelerates electron drift extraction into the ZnO buffer layer [26, 27, 28, 29, 30]. Beyond this interface, within the bulk of the ZnO thin film $0.90\ \mu m < x < 0.94\ \mu m$, the field drops instantly back to zero due to the potential saturation plateau, before final collection at the gold (Au) cathode.

Absorber doping therefore does not uniformly strengthen or weaken the internal electric field; it redistributes the electrostatic driving force spatially. Increasing the acceptor density progressively concentrates a larger fraction of the potential variation near the heterointerfaces and expands the quasi-neutral portion of the absorber, thereby shifting the relative contribution of drift- and diffusion-assisted transport. The optimum doping range should consequently be interpreted as the most favorable spatial balance between interfacial selectivity, bulk transport, and recombination rather than as the condition producing the highest local field intensity.

6.4. Recombination rates of the PV cell: ITO/NiO/$CH_3NH_3PbI_3$/ZnO/Au

Figure 6 presents the spatial distribution of the carrier recombination rates within the ITO/NiO/$CH_3NH_3PbI_3$/ZnO/Au device architecture for the different absorber acceptor doping concentrations ($10^{15}\ \mathrm{cm^{-3}}, 5 \times 10^{16}\ \mathrm{cm^{-3}}\ and\ 10^{18}\ \mathrm{cm^{-3}}$).

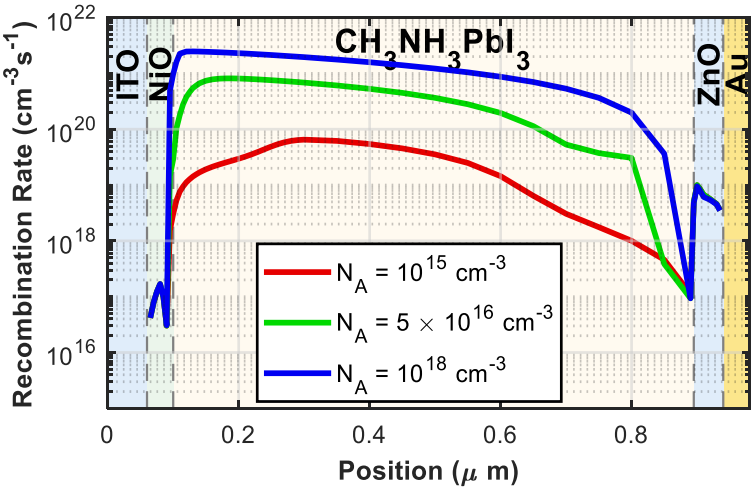


Figure 6 : Logarithmic carrier recombination rate profile for different doping levels of $CH_3NH_3PbI_3$

The investigation of **Figure 6** reveals a clear and substantial increase in the overall recombination rate as the doping concentration of the perovskite active layer rises. Within the active absorber region, the curve corresponding to a low doping level of $10^{15}\ cm^{-3}$ exhibits the lowest recombination values ($\sim 10^{15}\ cm^{-3}.s^{-1}$), whereas the highly doped profile at $10^{18}\ cm^{-3}.s^{-1}$ yields the highest loss magnitudes, particularly pronounced near the anodic $NiO/CH_3NH_3PbI_3$ interface, where the profiles exhibit a sharp peak before decaying progressively toward the cathodic $CH_3NH_3PbI_3/ZnO$ boundary. At the approach of this electron-selective interface, the recombination rate drops sharply by several orders of magnitude, reflecting efficient local charge extraction that depletes the interface of minority carriers and lowers the steady-state electron-hole product (n, p). Increasing background doping thus enhances electrostatic potential and transport properties while simultaneously accelerating recombination losses [31, 32].

6.5. Photogeneration rate of the PV cell: $ITO/NiO/CH_3NH_3PbI_3/ZnO/Au$

Figure 7 presents the spatial distribution of the photogeneration rate within the $ITO/NiO/CH_3NH_3PbI_3/ZnO/Au$ heterostructure under three distinct perovskite absorber acceptor doping concentrations ($10^{15}\ cm^{-3}, 5 \times 10^{16}\ cm^{-3}$ and $10^{18}\ cm^{-3}$).

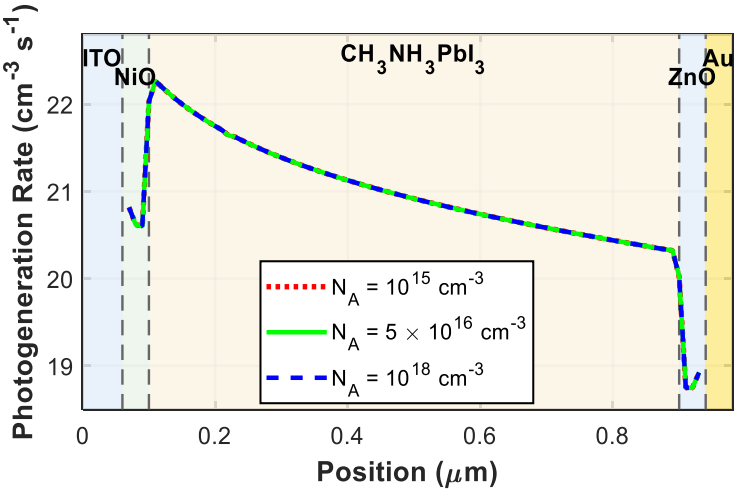


Figure 7 : Photogeneration rate profile across the device for different doping concentrations of the $CH_3NH_3PbI_3$ perovskite layer

The investigation of **Figure 7** reveals that the photogeneration-rate profiles are closely superimposed across the perovskite thickness for all three doping levels, confirming that absorber doping does not affect the optical absorption process or the resulting carrier-generation profile under the simulated conditions. The photogeneration rate rises sharply near the anodic $NiO/CH_3NH_3PbI_3$ interface, reaching a peak of approximately $2.33 \times 10^{22}\ cm^{-2}.s^{-1}$ at x=0.13 µm, then decays progressively consistent with Beer-Lambert attenuation of the incident photon flux down to approximately $1.87 \times 10^{22}\ cm^{-2}.s^{-1}$ near the $CH_3NH_3PbI_3/ZnO$ interface [33]. Because the generated-carrier population is essentially preserved across the doping range, the doping-induced changes in J_{sc}, FF, and η cannot be attributed to a modification of optical absorption; they instead originate from the subsequent transport, extraction, and recombination of the photogenerated carriers. The doping concentration therefore acts as an electrical control parameter governing carrier collection efficiency rather than the amount of carriers generated.

7. Effect of absorber doping on photovoltaic parameters and parasitic resistances

To gain a comprehensive understanding of the physical mechanisms governing the performance of the perovskite solar cell, the influence of the absorber layer doping concentration is systematically analyzed across the primary photovoltaic parameters alongside the series and shunt resistances. The joint variations of these quantities establish the direct correlations between carrier transport dynamics, resistive losses, and internal recombination pathways. The results are presented sequentially, beginning with the simultaneous evolution of the open-circuit voltage (V_{oc}), short-circuit current density (J_{sc}), fill factor (FF), and power conversion efficiency (η) in relation to the series (R_s) and shunt (R_{sh}) resistances.

7.1. Open-circuit voltage and series/shunt resistances

Figure 8 presents the simultaneous evolution of the open-circuit voltage and the parasitic resistances as a function of the perovskite absorber doping density, ranging from $10^{13}\ to\ 10^{18}\ cm^{-3}$

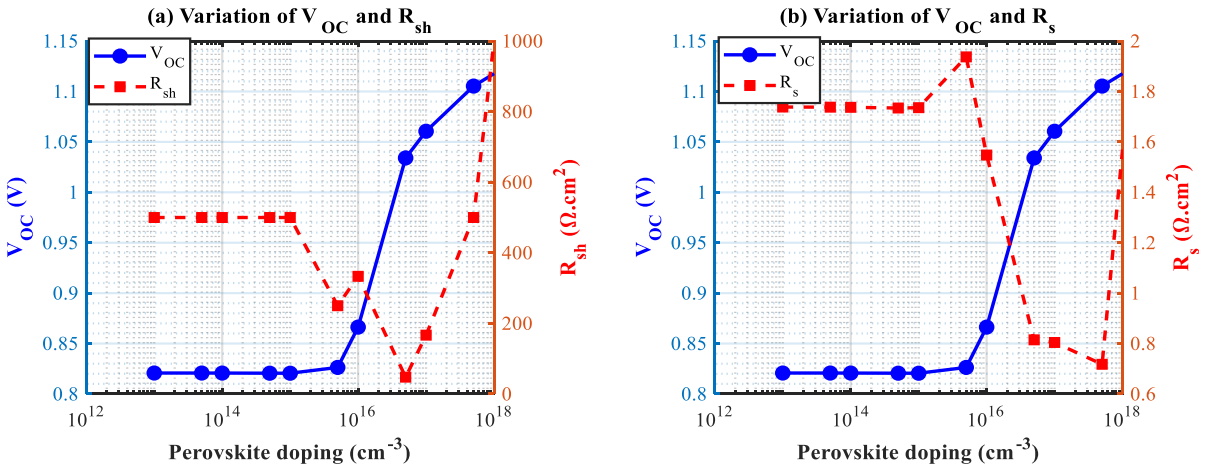


Figure 8 : Simultaneous variation of the open-circuit voltage (V_{oc}) and the series and shunt resistances (R_s, R_{sh}) as a function of doping

The analysis of the results demonstrates that V_{oc} increases progressively from 0.821 V at a doping concentration of $10^{13}\ cm^{-3}$ up to a maximum of 1.118 V at $10^{18}\ cm^{-3}$. This upward trend in voltage is accompanied by a global reduction in R_s up to a doping level of $10^{18}\ cm^{-3}$,

while R_{sh} remains moderate at low doping densities, decreases in the intermediate zone, and then rises sharply at the highest concentrations.

At low doping levels ($10^{13} - 10^{15}$ cm^{-3}), the relatively low V_{oc} values arise from the combined effects of a low majority-carrier density, a more spatially distributed potential drop, and a comparatively high effective transport resistance. Although R_{sh} is high ($\approx 500\ \Omega \cdot cm^2$), effectively suppressing parasitic leakage currents, the presence of a relatively high series resistance ($\approx 1.74\ \Omega \cdot cm^2$), restricts the efficiency of charge transport [24, 25, 34].

When the doping density is increased to 5×10^{16} cm^{-3}, V_{oc} rises sharply to reach 1.034 V, while R_s drops significantly, reflecting enhanced carrier transport and reduced ohmic losses. Although R_{sh} temporarily drops to $47.6\ \Omega \cdot cm^2$, this decrease does not penalize V_{oc} significantly.

For doping levels exceeding 10^{15} cm^{-3}, V_{oc} continues to rise toward 1.118 V, in parallel with a massive resurgence of R_{sh}, which reaches $1000\ \Omega \cdot cm^2$. Despite a slight rebound of R_s at the highest doping density, its influence remains secondary to the evolution of the junction electrostatics. The continued increase in open-circuit voltage is therefore better interpreted in terms of the doping-induced shift of the carrier quasi-Fermi levels and the associated electrostatic redistribution, rather than as evidence of a uniform reduction in recombination.

The increase in V_{oc} observed here does not imply that recombination is uniformly suppressed. Higher doping simultaneously modifies the quasi-Fermi-level splitting and junction electrostatics while increasing carrier losses in the absorber. These effects compete: the favorable electrostatic contribution dominates over part of the investigated range, whereas the recombination penalty progressively limits the voltage-related benefit and, more importantly, carrier collection at excessive doping.

7.2. Short-circuit current density and series/shunt resistances

Figure 9 illustrates the simultaneous evolution of the short-circuit current density and the series/shunt resistances as a function of the perovskite absorber doping density from 10^{13} cm^{-3} to 10^{18} cm^{-3}.

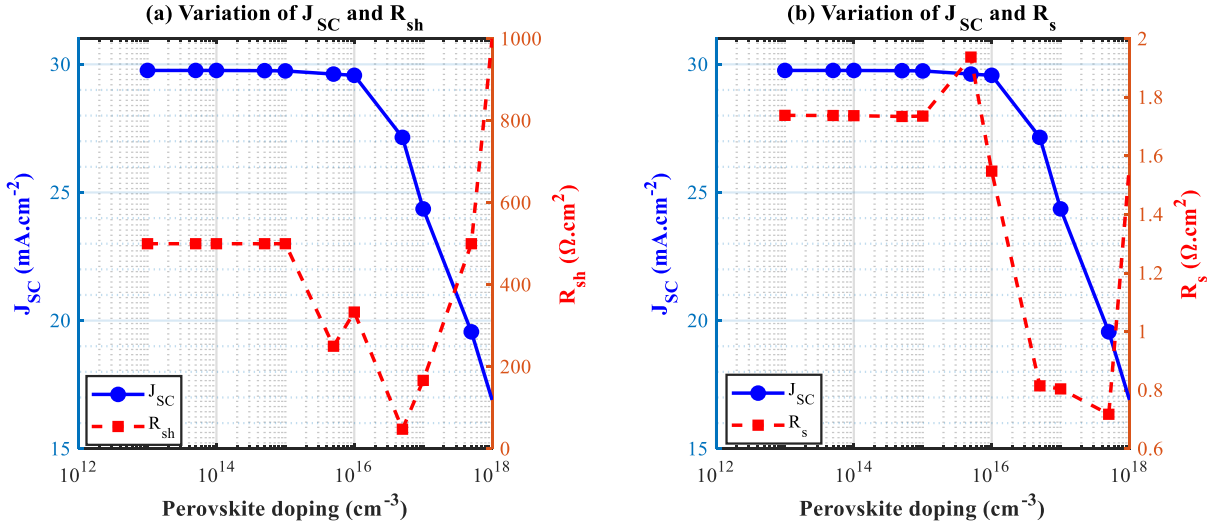


Figure 9 : Simultaneous variation of the short-circuit current density (J_{sc}) and the series and shunt resistances(R_s, R_{sh}) as a function of doping

The investigation of the profiles indicates that, in stark contrast to the open-circuit voltage behavior, J_{sc} increases progressively as the doping concentration decreases, ranging from $16.90\ to\ 29.76\ mA.\,cm^{-2}$ between 10^{18} cm^{-3} *and* 10^{13} cm^{-3}, because lower doping reduces

bulk recombination and allows a larger fraction of the photogenerated carriers to reach the collecting electrodes.

At low doping densities 10^{13} cm^{-3} – 10^{15} cm^{-3}, the series resistance remains relatively high ($R_s = 1.74\ \Omega \cdot cm^2$) while R_{sh} maintains elevated values ($\approx 500\ \Omega \cdot cm^2$), successfully constraining leakage currents, accounting for the high J_{sc} values. Conversely, as the doping level is increased, the majority carrier density becomes excessively high, severely accelerating Shockley-Read-Hall (SRH) and Auger recombination rates within the bulk absorber [27], depleting the free-carrier population available for the external photocurrent and degrading J_{sc} despite the lower R_s. Because the photogeneration profiles in **Figure 7** are essentially superimposed for all investigated doping levels, this strong decrease in short-circuit current at high doping cannot be attributed to reduced optical absorption. It instead provides direct evidence of a deterioration in carrier-collection probability caused by the combined effects of enhanced bulk recombination and the increasingly diffusion-dominated transport region.

7.3. Fill factor and series/shunt resistances

Figure 10 presents the evolution of the fill factor alongside the series and shunt resistances as a function of the perovskite absorber doping density from 10^{13} cm^{-3} *to* 10^{18} cm^{-3}.

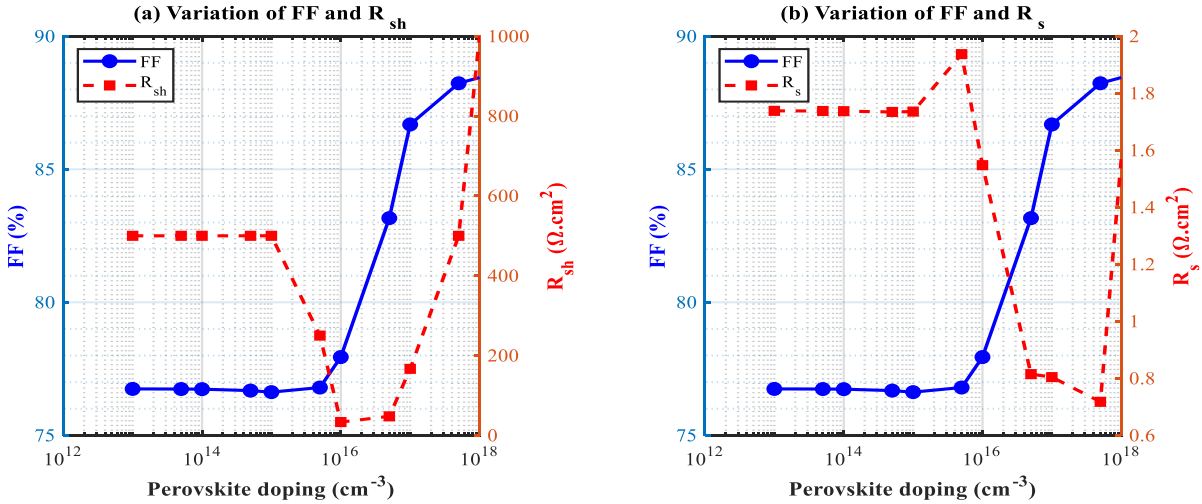


Figure 10 : Simultaneous variation of the fill factor (FF) and the series and shunt resistances (R_s, R_{sh}) as a function of doping

The results demonstrate that the fill factor increases progressively from 76.75% at a low doping of 10^{13} cm^{-3} up to a maximum value of 88.00% at 10^{18} cm^{-3}.

At low doping concentrations 10^{13} cm^{-3} *and* 10^{15} cm^{-3}, the fill factor remains relatively low ($\sim 76.5\%$) despite the high shunt resistance ($R_{sh} = 500\ \Omega.cm^2$), penalized by the high series resistance ($R_s = 1.74\ \Omega.cm^2$) [25, 34].

When the doping density increases up to 5×10^{15} cm^{-3}, the fill factor climbs rapidly to 83.16%, matching the sharp decline in series resistance. Although the shunt resistance drops simultaneously to approximately $47.6\ \Omega.cm^2$, its impact remains masked by the much larger gains from series resistance mitigation.

At heavily doped levels (10^{18} cm^{-3} – 10^{18} cm^{-3}), the fill factor continues to rise to its peak of 88.00%, despite a minor rebound of R_s to $1.57\ \Omega.cm^2$ at 10^{18} cm^{-3}, driven by the strengthening of the internal field and contact selectivity. The substantial increase of R_{sh}, to $1000\ \Omega.cm^2$ indicates a reduced sensitivity of the simulated J-V response to leakage-related losses rather than direct proof of fewer defects. Importantly, the doping level that maximizes

FF does not maximize the conversion efficiency: at the highest doping densities, the additional gain in FF is more than offset by the pronounced loss in J_{sc}. This decoupling confirms that FF alone cannot be used to define the optimal absorber doping.

7.4. Power conversion efficiency and series/shunt resistances

The conversion efficiency aggregates the responses of V_{oc}, J_{sc}., and FF. **Figure 11** presents the simultaneous evolution of the conversion efficiency and the parasitic resistances as a function of the perovskite doping density from 10^{13} cm^{-3} to 10^{18} cm^{-3}.

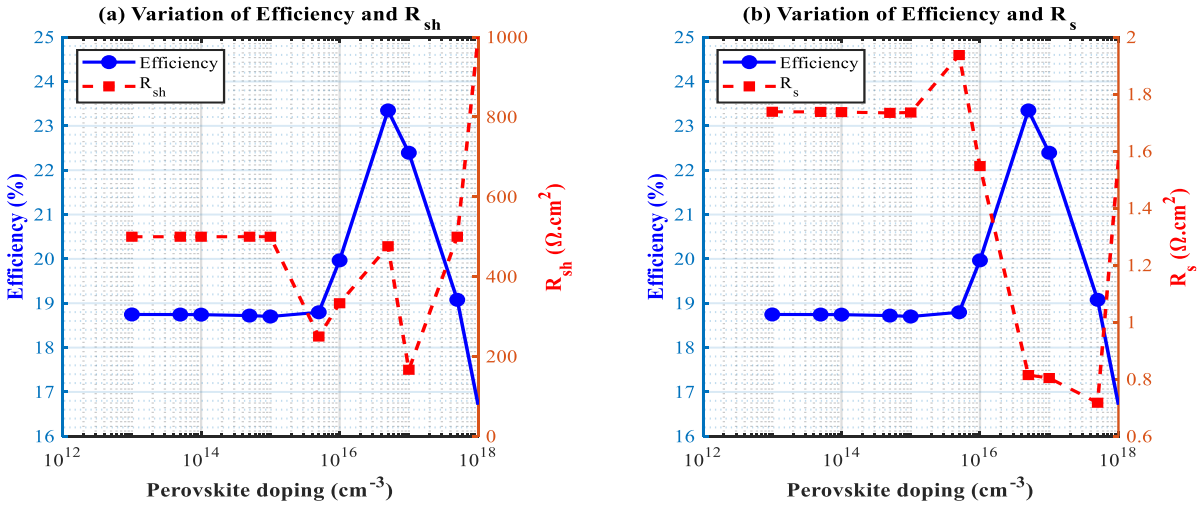


Figure 11 : Simultaneous variation of the power conversion efficiency (η) and the series and shunt resistances (R_s, R_{sh}) as a function of doping

The results demonstrate that the efficiency increases progressively as the doping concentration rises from 10^{13} cm^{-3} to 5×10^{16} cm^{-3}, reaching a peak value of 23.35%, before undergoing a steady decline at higher doping thresholds [21, 24, 25, 35].

At low doping thresholds, the efficiency remains constrained despite the high shunt resistance. In this regime, the electrostatic potential drop is distributed over a broad region rather than strongly localized at the selective interfaces, while the comparatively high effective series resistance ($\approx 1.74\ \Omega.\,cm^2$) limits carrier extraction and the electrical power delivered by the device [35].

When the doping level is optimized at 5×10^{16} cm^{-3}, the conversion efficiency rises because the device reaches the most favorable simultaneous balance of transport, electrostatics, and recombination, while the effective series resistance approaches its minimum R_s, reducing transport-related voltage losses [21]. Although R_{sh} decreases to around $47.6\ \Omega.\,cm^2$, the improvement associated with lower effective series resistance and better interfacial selectivity remains sufficient to outweigh leakage-related losses, yielding the maximum efficiency of 23.35%. Beyond this point, the rapid decline of J_{sc} caused by enhanced recombination becomes dominant, even though V_{oc} and FF may continue to improve.

7.5. Overall physical interpretation of the doping-induced performance trade-off

Taken together, the results identify absorber doping as an electrical-control parameter that leaves the optical generation profile essentially unchanged but reorganizes the electrostatic environment in which photogenerated carriers are transported. The device evolves from a low-doping regime characterized by an extended potential drop and comparatively high transport resistance, through an intermediate regime in which conductivity, interfacial selectivity, and carrier collection are favorably balanced, toward a high-doping regime characterized by

strongly localized interfacial fields, a larger diffusion-dominated bulk region, and rapidly increasing recombination. The resulting efficiency maximum is therefore a transport–recombination crossover rather than the extremum of any single electrical quantity. In particular, it does not coincide with the lowest recombination rate, the largest V_{oc}, the highest J_{sc}, or the strongest local electric field considered independently. It instead marks the best global compromise among electrostatic driving force, resistive transport, carrier collection, and recombination losses.

8. Conclusion

This numerical study evaluates how absorber-layer ($CH_3NH_3PbI_3$) doping reshapes the electrical and photovoltaic response of a planar perovskite solar cell simulated with SILVACO TCAD ATLAS. Beyond identifying an optimal doping level, the analysis shows that doping controls the spatial distribution of the electrostatic potential and internal field and thereby changes the relative importance of drift-assisted transport, diffusion-assisted collection, resistive losses, and recombination throughout the heterostructure.

Increasing the acceptor density initially improves the electrical response by lowering the effective series resistance and concentrating the electrostatic potential drop near the selective interfaces. This favors carrier selectivity and extraction over the low-to-intermediate doping range. At excessive doping, however, the quasi-neutral bulk region becomes more dominant and SRH/Auger recombination rises sharply; the resulting loss of carrier collection, reflected by the decrease in short-circuit current, eventually outweighs the conductivity-related benefits. The optimum efficiency therefore arises from a crossover between transport enhancement and recombination loss rather than from a monotonic strengthening of the internal field.

The ultimate performance trade-off is achieved at an optimal perovskite doping concentration of 5×10^{16} cm^{-3}. At this threshold, the device delivers a peak power conversion efficiency of 23.35%, a fill factor of 83.16%, an open-circuit voltage of 1.034 V, and a short-circuit current density of $27.15\ mA.cm^{-2}$, defining a physically grounded doping-design window for balancing electrostatic carrier extraction and recombination losses in planar perovskite solar cells. The same analysis framework may subsequently be extended to more complex device architectures, but such extensions require dedicated simulations.

Statements and Declarations

Funding :

The authors declare that no funds, grants, or other support were received during the preparation of this manuscript.

Competing Interests :

The authors have no relevant financial or non-financial interests to disclose.

Data Availability

The simulation data and analysis results generated during the current study are available from the corresponding author upon reasonable request.

Ethics approval and consent to participate

Not applicable.

Consent for publication

Not applicable.

Author Contributions

AT contributed to the conception and design of the study, numerical simulations, data analysis, interpretation of the results, and preparation of the manuscript. FS contributed to the analysis and interpretation of the simulation results and critically revised the manuscript. DD contributed to the analysis of the results and the critical revision of the scientific content. AMY contributed to the scientific interpretation and critical revision of the manuscript. MLS supervised the research, provided scientific guidance, and contributed to the final validation of the manuscript. All authors reviewed and approved the final version of the manuscript and agreed to be accountable for all aspects of the work, ensuring that questions related to the accuracy or integrity of any part of the study are appropriately investigated and resolved.

References

[1] Coulibaly A.B., Oyedele S.O., Kre N.R., Aka B. (2019). Comparative study of lead-free perovskite solar cells using different hole transporter materials, *Model. Numer. Simul. Mater. Sci.*, 9(4), 97–107. https://doi.org/10.4236/mnsms.2019.94006

[2] Li W., Sha T., Wang Y., Yu W., Jiang K., Zhou H., Liu C., Hu Z., Chu J. (2017). Effects of deposition methods and processing techniques on band gap, interband electronic transitions, and optical absorption in perovskite CH3NH3PbI3 films, *Appl. Phys. Lett.*, 111(1), 011906. https://doi.org/10.1063/1.4991864

[3] Zaman M.A., Akhtaruzzaman M., Rashid M.J. (2019). Influence of electron transport layer on the performance of perovskite solar cell, *Proc. ICIET*, 2019, 1–7. https://doi.org/10.1109/ICIET48527.2019.9290690

[4] De Los Santos I.M., Cortina-MarreroH.J., Ruíz-Sánchez M.A., Hechavarría-Difur L., Sánchez-Rodríguez F.J., Courel M., Hu H. (2020). Optimization of CH3NH3PbI3 perovskite solar cells: A theoretical and experimental study, *Sol. Energy*, 199, 198–205. https://doi.org/10.1016/j.solener.2020.02.026

[5] Silvaco International. (2011). *ATLAS user's manual: Device simulation software* (Version 5.12.1). Silvaco International. https://www.silvaco.com

[6] Correa-Baena J.-P., Saliba M., Buonassisi T., Grätzel M., Abate A., Tress W., Hagfeldt A. (2017). Promises and challenges of perovskite solar cells, *Science*, 358(6364), 739–744. https://doi.org/10.1126/science.aam6323

[7] Park S.Y., Zhu K. (2022). Progress concerning SnO2 for efficient and stable n–i–p perovskite solar cells, *Adv Mater.*, 34(27), 2110438. https://doi.org/10.1002/adma.202110438

[8] Lun S.-X., Wang S., Yang G.-H., Guo T.-T. (2015). A new explicit double-diode modelling method based on Lambert W-function for photovoltaic arrays, *Sol. Energy*, 116, 69–82. https://doi.org/10.1016/j.solener.2015.03.043

[9] Song Z., Fang K., Sun X., et al. (2021). An effective method to accurately extract the parameters of the single diode model of solar cells, *Nanomaterials*, 11(9), 2615. https://doi.org/10.3390/nano11092615

[10] Green M.A. (1981). Solar cell fill factors: General graph and empirical expressions, *Solid-State Electron.*, 24(8), 788–789. https://doi.org/10.1016/0038-1101(81)90062-9

[11] Yang W.S., Park B.-W., Jung E.H., Jeon N.J., Kim Y.C., Lee D.U., Shin S.S., Seo J., Kim E.K., Noh J.H., Seok S.I. (2017). Iodide management in formamidinium-lead-halide-based perovskite layers for efficient solar cells, *Science*, 356(6345), 1376–1379. https://doi.org/10.1126/science.aan2301

[12] Shariah A., Mahasneh F. (2022). Emitter layer optimization in heterojunction bifacial silicon solar cells, *J. Semicond.*, 43(12), 122701. https://doi.org/10.1088/1674-4926/43/12/122701

[13] Davis J.A., Boscardin M., Crivellari M., Fanò L., Large M., Menichelli M., Morozzi A., Moscatelli F., Movileanu-Ionica M., Passeri D., Petasecca M., Piccini M., Rossi A., Scorzoni A., Thompson B., Verzellesi G., Wyrsch N. (2020). Modeling a thick hydrogenated amorphous silicon substrate for ionizing radiation detectors, *Front. Phys.*, 8, 158. https://doi.org/10.3389/fphy.2020.00158

[14] Chang S.T., Hsieh B.F., Liu Y.C. (2012). A simulation study of thin film tandem solar cells with a nanoplate absorber bottom cell, *Thin Solid Films*, 520(8), 3369–3373. https://doi.org/10.1016/j.tsf.2011.10.094

[15] Sikder M.D., Mamur H., Bhuiyan M.R.A. (2025). Optimizing layer configuration and material selection to enhance CIGS solar cell performance through computational simulation, *Hybrid Adv.*, 10, 100460. https://doi.org/10.1016/j.hybadv.2025.100460

[16] Uddin M.S., Hosen R., Sikder S., Mamur H. (2024). Photovoltaic performance enhancement of Al/ZnO:Al/i-ZnO/CdS/CIGS/Pt solar cell using SCAPS-1D software, *Next Energy*, 2, 100080. https://doi.org/10.1016/j.nxener.2023.100080

[17] Cotfas D.T., Cotfas P.A., Kaplanis S. (2013). Methods to determine the DC parameters of solar cells: A critical review, *Renew. Sustain. Energy Rev.*, 28, 588–596. https://doi.org/10.1016/j.rser.2013.08.017

[18] Hegedus S.S., Shafarman W.N. (2004). Thin-film solar cells: Device measurements and analysis, *Prog. Photovolt. Res. Appl.*, 12(2–3), 155–176. https://doi.org/10.1002/pip.518

[19] Al-Asbahi A., Qaid S.M.H., Hezam M., Bedja I., Ghaithan H.M., Aldwayyan A.S. (2020). Effect of deposition method on the structural and optical properties of CH3NH3PbI3 perovskite thin films, *Opt. Mater.*, 103, 109836. https://doi.org/10.1016/j.optmat.2020.109836

[20] Lv Y., Zhang H., Wang J., Chen L., Bian L., An Z., Qian Z., Ren G., Wu J., Nüesch F., Huang W. (2020). All-in-One Deposition to Synergistically Manipulate Perovskite Growth for High-Performance Solar Cell, *Research*, 2020, 2763409. https://doi.org/10.34133/2020/2763409

[21] Sunny A., Rahman S., Khatun M.M., Al Ahmed S.R. (2021). Numerical study of high performance HTL-free CH3NH3SnI3-based perovskite solar cell by SCAPS-1D, *AIP Adv.*, 11, 065102. https://doi.org/10.1063/5.0049646

[22] Abdelaziz S., Zekry A., Shaker A., Abouelatta M. (2020). Investigating the performance of formamidinium tin-based perovskite solar cell by SCAPS device simulation, *Opt. Mater.*, 101, 109738. https://doi.org/10.1016/j.optmat.2020.109738

[23] Hima A., Le Khouimes A.K., Rezzoug A., Ben Yahkem M., Khechekhouche A., Kemerchou I. (2019). Simulation and optimization of CH3NH3PbI3 based inverted planar heterojunction solar cell using SCAPS software, *Int. J. Energetica*, 4(1), 56–59. https://doi.org/10.47238/ijeca.v4i1.92

[24] Jeyakumar R., Bag A., Nekovei R., Radhakrishnan R. (2020). Influence of electron transport layer (TiO2) thickness and its doping density on the performance of

CH3NH3PbI3-based planar perovskite solar cells, *J. Electron. Mater.*, 49(6), 3533–3539. https://doi.org/10.1007/s11664-020-08041-w

[25] Marand Z.R., Kermanpur A., Karimzadeh F., Barea E.M., Hassanabadi E., Halvani Anaraki E., Julián-López B., Masi S., Mora-Seró I. (2020). Structural and electrical investigation of cobalt-doped NiOx/perovskite interface for efficient inverted solar cells, *Nanomaterials*, 10(5), 872. https://doi.org/10.3390/nano10050872

[26] Miller E.M., Zhao Y., Mercado C.C.,Saha S.K., Luther J.M., Zhu K., Stevanović V., Perkins C.L., van de Lagemaat J. (2014). Substrate-controlled band positions in CH3NH3PbI3 perovskite films, *Phys. Chem. Chem. Phys.*, 16(40), 22122–22130. https://doi.org/10.1039/C4CP03533J

[27] Wang J., Wang H.-L. (2023). Recent progress in electrode interface modification of perovskite solar cells, *Mater. Chem. Front.*, 7(22), 5731–5743. https://doi.org/10.1039/D3QM00610G

[28] Xiao T., Xu K. (2026). Recent progress in enhancing built-in electric fields of perovskite solar cells via junction engineering, *Beilstein J. Nanotechnol.*, 17, 602–621. https://doi.org/10.3762/bjnano.17.42

[29] Cheng J., Cao H., Zhang S., Yue F., Zhou Z. (2024). Reinforcing built-in electric field to enable efficient carrier extraction for high-performance perovskite solar cells, *Mater. Chem. Front.*, 8(4), 956–985. https://doi.org/10.1039/D3QM00956D

[30] Thakur A., Raj M., Deupa M., Surapaneni R., Gupta S., Goel N. (2025). Review and perspectives of perovskite solar cells: Toward environmentally sustainable and efficient photovoltaics, *Energy Fuels*, 39(51), 24012–24044. https://doi.org/10.1021/acs.energyfuels.5c05018

[31] Ahmed N.u.A., Mura M.L., Kuzhir P., Karpicz R., Tucci V., Lamberti P. (2026). Modelling of Electrodes in Perovskite Solar Cells for Aerospace Applications, *Eng. Proc.*, 133(1), 68. https://doi.org/10.3390/engproc2026133068

[32] Mehrabian M., Taleb-Abbasi M., Akhavan O. (2024). Using Cu2O/ZnO as two-dimensional hole/electron transport nanolayers in unleaded FASnI3 perovskite solar cells, *Materials*, 17(5), 1064. https://doi.org/10.3390/ma17051064

[33] Mehrabian M., Norouzzadeh P., Akhavan O. (2026). Improving hybrid perovskite solar cells by utilization and optimization of Cs2AgBiBr6/MAPbI3/CsSnI3 triple cascade structure, *J. Power Sources*, 661, 238633. https://doi.org/10.1016/j.jpowsour.2025.238633

[34] Jung K., Lee J., Kim J., Chae W.-S., Lee M.-J. (2016). Solution-processed flexible planar perovskite solar cells: A strategy to enhance efficiency by controlling the ZnO electron transfer layer, PbI2 phase, and CH3NH3PbI3 morphologies, *J. Power Sources*, 324, 142–149. https://doi.org/10.1016/j.jpowsour.2016.05.026

[35] Ahmed M.I., Hussain Z., Mujahid M., Khan A.N., Javaid S.S., Habib A. (2016). Low resistivity ZnO:GO electron transport layer based CH3NH3PbI3 solar cells, *AIP Adv.*, 6, 065339. https://doi.org/10.1063/1.4953397